VIRTUAL AND PHYSICAL PROTOTYPING
2024, VOL. 19, NO. 1, e2397008 (20 pages)
https://doi.org/10.1080/17452759.2024.2397008

Taylor & Francis
Taylor & Francis Group

Knowledge-based bidirectional thermal variable modelling for directed energy deposition additive manufacturing

Jian Qin[a], Pradeeptta Taraphdar[a], Yongle Sun[a], James Wainwright[a], Wai Jun Lai[a], Shuo Feng[a], Jialuo Ding[a,b] and Stewart Williams[a]

[a]Welding and Additive Manufacturing Centre, Cranfield University, Cranfield, UK; [b]WAAM3D Limited, Milton Keynes, UK

ABSTRACT

Directed energy deposition additive manufacturing (DED-AM) has gained significant interest in producing large-scale metallic structural components. In this paper, a knowledge-based machine learning (ML) approach, combining both physics-based simulation and data-driven modelling, is proposed for a study on thermal variables of DED-AM. This approach enables both forward and backward predictions, which breaks down the barriers between the basic process parameters and key process attributes. Process knowledge plays a critical role to enable the prediction and enhance the accuracy in both prediction directions. The proposed ML approach successfully predicted the thermal variables of wire arc based DED-AM for forward modelling and the process parameters for backward modelling, typically within 7% errors. This approach can be further generalised as a powerful modelling tool for design, control, and evaluation of DED-AM processes regarding build geometry and properties, as well as an essential constituent element in a digital twin of a DED-AM system.

ARTICLE HISTORY
Received 6 March 2024
Accepted 21 August 2024

KEYWORDS
Directed energy deposition additive manufacturing (DED-AM); digital manufacturing; knowledge-based data-driven modelling; machine learning (ML); finite element analysis (FEA)

1. Introduction

1.1. Background

Directed energy deposition additive manufacturing (DED-AM) applies intensive single or multiple heat sources to melt feedstock with directed energy, successively depositing the molten material on to a substrate or previously deposited layer to build a part [1]. Dependent on build requirements, such as material properties, deposition rate and geometry of the part, there are diverse types of heat sources that can be utilised, including electric arc, laser beam, electron beam and their combinations. By adopting this cutting-edge technology, a dramatic cost reduction can be achieved. For example, Boeing expects to save USD 2–3 million per aeroplane by using DED-AM built parts [2]. Due to its unique processing characteristics, DED-AM becomes increasingly popular in many industries such as aerospace, oil & gas, nuclear, automotive, and shipbuilding [3].

Thermal variables, in terms of cooling rates, temperature gradients, and melting isotherms, are fundamentally important, which determine the material properties and performance of a DED-AM built part. The control of thermal variables directly influences the temperature distribution within the build, affecting the solidification rate [4], grain growth [5], residual stress and distortion [6,7]. Precise control of these variables enables the optimisation of deposition parameters, leading to improved metallurgical properties, reduced distortion, and enhanced part quality. Due to the rapid heating, melting, and solidification caused by a moving heat source like an arc, laser or electron beam, diverse regions in the part undergo repeated thermal cycles, impacting their local characteristics. Variable thermal cycles create non-uniform microstructure leading to inconsistent mechanical properties [8]. During DED-AM, temperature measurements are limited to accessible surfaces, but not the melt-pool or solid part interior. Detailed 3D temperature distribution is essential for identifying crucial factors affecting part quality, such as cooling rates, solidification conditions, microstructures, and residual stresses. The growth rate of the local solidification front, and the temperature gradient at the solid–liquid interface, are vital for the mode of solidification. Their ratio determines the solidification morphology as either planar, cellular, or dendritic, while the cooling rate influences the size and constituents of the microstructure [9]. Rapid heating and cooling in AM cause steep slopes in time-temperature graphs, indicating high heating and cooling rates. Cooling rates differ based on the target alloy and

CONTACT Yongle Sun Yongle.Sun@cranfield.ac.uk Welding and Additive Manufacturing Centre, Cranfield University, Cranfield MK40 3AA, UK

measurement location. A single cooling rate does not fit all AM thermal cycles, as it varies with temperature and location. Thus, 3D temperature fields are essential for comprehending the part microstructure and properties following the fundamental physics [10].

1.2. Finite element analysis (FEA) for thermal variable in DED-AM

Temperature measurement in DED-AM is always challenging due to rapidly moving heat sources and transient temperature changes. Temperature sensors, such as thermocouples, are commonly used away from the molten area, and thin thermocouples are required to minimise errors. They offer local temperature measurements but fail to provide a complete temperature field. Infrared thermography captures surface temperatures but lacks 3D full field data [11]. Due to the challenges of measuring the temperature field, digital modelling becomes a tool for simulating the process and predicting the 3D temperature field. FEA is one of the most commonly used digital methods for modelling thermal variables [12]. FEA simulates the heat transfer phenomena and predicts the temperature field during the DED-AM process. It enables designers and engineers to analyse different process parameters, material properties, and cooling strategies to achieve desired microstructures and minimised defects (e.g. cracks and distortion). By accurately predicting thermal behaviour, FEA aids in optimising build strategies, reducing experimental trial and error, and ensuring the quality and reliability of the final parts in DED-AM processes. FEA also helps in identifying potential failure zones, ensuring structural integrity, and speeding up process development. However, like other physics-based solutions, FEA modelling generally requires intense computational resource and takes long time for part-scale simulation.

One common challenge in FEA models for DED-AM is the high computational costs due to the mismatch between the sizes of the heat source, deposited layer and built part [13, 14]. The heat source is much smaller than the part, causing a significant difference in time and length scales. This difference requires fine spatial/temporal discretisation for accurate numerical solutions, making the models computationally intensive. A ‘steady-state’ model was proposed by Ding et al. [15] to improve computational efficiency, assuming a stable thermal state during long-wall deposition. Accurate modelling also often involves complex transient analysis that considers various physics such as arc behaviour, heat transfer, solidification, and stress evolution. However, due to computational limitations, these multi-physics simulations are usually confined to small domains and short time. To model part-level stress and distortion, simplifications are necessary. Approaches like the inherent strain method [16], lumping technique, and peak temperature method have been adapted from welding applications [17]. Martukanitz et al. [18] demonstrated progress in integrated computational systems for AM, using adaptive octree-based meshes for quick thermal stress simulation. Li et al. [19] and Denlinger et al. [20] proposed multi-scale FEA techniques for metal deposition, resulting in distortion predictions close to experimental results. Whilst simplified models generally capture trends and achieve reasonable estimation, complex geometries and diverse deposition paths remain a challenge.

1.3. Machine learning (ML) for surrogate modelling in DED-AM

Exploiting digital and artificial intelligence technologies, such as ML, becomes a critical research topic to support FEA modelling [21]. Many researchers have applied ML technologies into their research due to its irreplaceable benefits and advantages, such as no data attribute limitation, low computational resource requirement, and ease to integrate with other digital methods. This involves leveraging datasets from experiments and validated simulations. The focus of ML is the modelling of data and generating reliable predictions for tasks involving regression and classification [22]. The application of modern deep learning (DL) techniques has showcased considerable benefits across diverse domains, encompassing material design and various aspects of manufacturing processes [23]. Leveraging the power of ML and DL, researchers have effectively created surrogate models (SM) for forecasting thermal profiles in AM. For instance, Pham et al. [24] developed a simple ML-based SM to predict temperature and melt pool size in a 36-layer DED-AM process for a cubic part. Validated FEA simulations and experimental data were used for model training. Fetni et al. [25] conducted a thorough investigation using artificial neural networks to predict various thermal profiles in DED-AM of 316L stainless steel and tungsten carbides. Their models achieved accuracy levels surpassing 99% and offered rapid predictions. Zhu et al. [23] introduced the initial application of a physics-informed neural network (PINN) for predicting temperature and melt pool fluid dynamics in metal AM. The study was carried out incorporating PINN on two key AM scenarios, demonstrating its precise predictions with limited labelled training data. Roy and Wodo [26] also developed an SM to predict the thermal behaviour of an AM process. Using fused-filament fabrication (FFF) as an example, the model, derived from physics-based data, achieved over 95% accuracy and was 1000 times faster than the original model. The ML technology has been proven to enable the development of highly accurate surrogate models for predicting thermal profiles and melt pool dynamics, demonstrating both precision and computational efficiency.

Currently, in ML modelling research, the emphasis is primarily placed on thermal variables as the outputs of the model. These thermal variables represent the temperature distribution or other heat-related characteristics in each system or process. The inputs to these models typically consist of basic process parameters such as power, wire feed speed, and travel speed. This approach, often referred to as forward modelling, aims to predict the thermal behaviour of the system based on the known process parameters. However, in practical scenarios where the process is being designed, the inverse relationship is often required. Instead of predicting the thermal variables from the process parameters, engineers or researchers may need to determine the appropriate process parameters based on the desired thermal variables. This is known as reverse modelling or backward modelling [27]. This backward modelling plays a vital role in process design. By studying bidirectional modelling, researchers gain a comprehensive understanding of the relationship between process parameters and thermal variables, enabling accurate prediction and optimisation of system behaviour. It is also much more efficient compared to conventional optimisation and evolutionary approaches, including genetic algorithms, particle swarm optimisation, and ant colony optimisation. Such high efficiency is essential for real-time simulation and online control.

1.4. Bidirectional modelling for process study

Bidirectional modelling not only facilitates the accurate prediction of thermal variables for given process parameters but can also allow the determination of process parameters to meet predefined requirements. Xiong et al. [28] adopted a neural network as the main method for the bead geometry prediction. To forecast process parameters precisely according to the desired bead geometry, the forward neural network model needed to work with a backward prediction strategy. In the reverse model, only two input features of layer width and height geometry were used to obtain four output process parameters. Some assumptions were made to solve this issue in their research, such as fixing the less related feature (e.g. nozzle-to-plate distance) and optimisation of the results by changing the process parameters. These assumptions make the entire simulation a time-consuming process involving numerous iterations. Ding et al. [29] designed and developed an intelligent weld bead modelling system for wire + arc additive manufacturing (WAAM), which can guide WAAM engineers and operators to select the suitable process parameters. The proposed modelling system consisted of three main sections, i.e. data generation section, model creation section, and welding parameter generation section, which were implemented through a general ML modelling route. The support vector machine (SVM) was applied as the core ML modelling algorithm. In their research, a bidirectional modelling approach was also proposed. In the forward modelling, three process parameters, including wire feed speed, travel speed and inter-pass temperature, were used as the input to predict the bead height and overlapping distance. In backward modelling, the desired overlapping distance and bead height were used to predict only one process parameter. For each process parameter prediction, the other two parameters were fixed to mitigate issues associated with the data dimension of the modelling.

The current bidirectional modelling strategy typically requires larger and more diverse datasets than unidirectional modelling, posing challenges in data acquisition and preparation. There is also a risk of overfitting when working with limited or imbalanced datasets. Moreover, interpreting the results of bidirectional models can be also challenging due to the complex relationships and causalities between input and output variables. Given these drawbacks, incorporating knowledge-based ML approaches could help overcome these challenges and harness the benefits of bidirectional modelling. By integrating domain knowledge and expertise into the modelling process, these drawbacks can be mitigated. Knowledge-based ML can help simplify the complexity by guiding the selection of relevant features and designing interpretable models. Additionally, leveraging prior knowledge can aid in addressing data limitations and reduce the risk of overfitting. By combining the power of data-driven learning with domain knowledge, we can enhance the interpretability, efficiency, and reliability of bidirectional models, enabling us to unlock their full potential in various applications [30]. Ko et al. [31] developed a framework which integrated the process knowledge to Design for Additive Manufacturing (DfAM) based on knowledge graph ML. The AM design rules, principles, and fundamentals were formatted as the knowledge structure. The knowledge-based features were extracted from the AM database which is based on the pre-defined knowledge structure. The knowledge can also assist the ML modelling for reducing the redundant data contained in the data-driven model. However, applying knowledge-based ML technologies in AM is still scarce in the literature, and the relevant papers for DED-AM are even fewer. There is a research gap in using knowledge-based ML modelling for solving DED-AM issues.

In this paper, we present a novel digital approach that integrates ML and FEA modelling techniques. This approach is specifically designed to address the challenges of modelling thermal variables in DED-AM processes. We leverage knowledge-based process factors, such as heat input, energy density, and material feed, to fully exploit the potential of digital technologies in tackling these challenges. To achieve this, we develop a knowledge-based ML modelling framework that enables bidirectional predictions. In the forward direction, we utilise the initial model inputs, which consist of basic process parameters like arc current, travel speed, and wire feed speed. Additionally, we incorporate advanced model inputs derived from knowledge-based process factors. Through training using FEA output data, the ML model predicts the thermal variables. In the backward direction, the ML model first predicts the process factors based on the desired process attributes and then derive the process parameters from the knowledge-based features. Both forward and backward predictions have significant implications for understanding, analysing, designing, and optimising DED-AM processes. To address computational and data management challenges, we focus on defining and collecting key thermal variables that have a dominant influence on metallurgical and mechanical responses. This selection is guided by physics-based principles and requirements. By doing so, we effectively reduce the computational burden and streamline the data management in this framework. Through this proposed digital approach, we aim to leverage the strengths of ML and FEA modelling techniques, informed by knowledge-based process factors, to enhance our understanding and control of thermal variables in DED-AM processes.

2. Thermal FEA modelling

Before introducing the details of the methodology, the list of nomenclature is displayed in Table 1.

The thermal variables are focused to study the process attributes, including cooling rate, temperature gradient, and isotherms of the local area surrounding the melt pool. The thermal variable dataset was obtained from FEA. The FEA model was developed based on previous experiments of a plasma WAAM process, in which Ti-6Al-4V alloy was deposited to build straight walls [32]. WAAM is a major DED-AM variant for structural component building. The experimental data used for generating the FEA models was collected for 26 deposited walls, which followed the Design of Experiments method to ensure the representativeness of the data. A wide range of process parameters and the associated wall geometry data were considered, including wire feed speed of $20 - 100\ \mathrm{mm/s}$, arc torch travel speed of $2 - 10\ \mathrm{mm/s}$ and arc current of $120 - 300\ \mathrm{A}$, as well as the corresponding average wall width of $5.9 - 16.6\ \mathrm{mm}$ and layer height of $0.7 - 2.1\ \mathrm{mm}$, see Appendix A for details.

A series of thermal FEA models were generated based on the plasma arc process parameters and wall geometry reported in Martina et al.'s work [32, 33]. The walls were made of fourteen Ti-6Al-4V layers with a length of 140 mm. The width and height of the wall varied

Table 1. List of nomenclature used in this research.

Abbreviation	Meaning	Abbreviation	Meaning
DED-AM	Directed energy deposition additive manufacturing	**ML**	Machine learning
AM	Additive manufacturing	**3D**	Three dimensional
FEA	Finite element analysis	**DL**	Deep learning
SM	Surrogate model	**PINN**	Physics-informed neural network
DfAM	Design for additive manufacturing	**ANN**	Artificial neural network
SVM	Support vector machine	**WAAM**	Wire arc additive manufacturing
WFS	Wire feed speed	**TS**	Travel speed
q	Body heat flux	Q_T	Total power of the arc
η	Arc efficiency	a_f	Front heat source radius
a_r	Rear heat source radius	**U**	Power source voltage
C	Power source current	**T**	Temperature
t	Time	$Cov(X, Y)$	Covariance between two features
σ_X	Standard deviation of one feature	Q_{linear}	Linear heat input
$D_{volumetric}$	Volumetric energy density	A_{wire}	Cross-sectional area of the wire
r_{wire}	Radius of the wire	$S_{deposition}$	Deposited layer area
$R_{deposition}$	Deposition rate	ρ	Material density
PCC	Pearson correlation coefficient	**RMSE**	Root mean square error
p_i	Prediction data	$\bar{p}$	Average value of the prediction data
a_i	Actual data	$\bar{a}$	Average value of the entire data

between the 26 samples deposited using different process parameters. The substrate plate measured 200 mm × 100 mm × 7 mm. The thermal model employed the efficient Eulerian approach [15] to obtain the steady-state temperature field and the associated thermal variables. An interlayer temperature of 100 $^\circ C$ was adopted in the simulation using the Abaqus software package.

2.1. FEA model setup

Figure 1 shows the FEA model setup for one typical WAAM deposited wall. A double ellipsoidal heat source [34] was positioned in a region discretised with a refined mesh and kept stationary during the simulation, while a mass flow rate equal to the product of material density and torch travel speed was assigned to the whole model. The effect of heat source motion was captured through mass flow from the inlet face to the outlet face. This approach typically reduces the computational time by two orders of magnitude compared to the transient thermal model based on the Lagrangian approach [15]. Forced convection/diffusion brick elements (Abaqus designation: DCC3D8) were used in the WAAM model, and further refining of the mesh did not change the results. The temperature-dependent material properties for Ti-6Al-4V were adopted from Ding's work [35]. It should be noted that an artificially high thermal conductivity was assumed when temperature exceeded the melting point, thereby approximating the heat transfer through the liquid metal flow in the melt pool.

The centre of the double ellipsoid heat source is indicated by the coordinates (x_0, y_0, z_0). The body heat flux q in the front ($x < x_0$) of the heat source can be expressed as.

$$q = \frac{6\sqrt{3} f_f \eta Q_T}{a_f b c \pi \sqrt{\pi}} e^{-3(x-x_0)^2/a_f^2} e^{-3(y-y_0)^2/b^2} e^{-3(z-z_0)^2/c^2} \tag{1}$$

In the rear ($x > x_0$) of the heat source, the expression is

$$q = \frac{6\sqrt{3} f_r \eta Q_T}{a_r b c \pi \sqrt{\pi}} e^{-3(x-x_0)^2/a_r^2} e^{-3(y-y_0)^2/b^2} e^{-3(z-z_0)^2/c^2} \tag{2}$$

where Q_T is the total power of the arc, and η is the arc efficiency (i.e. energy absorption efficiency for the arc); a_f and a_r are the heat source radii in the front and rear, respectively, and b and c are the heat source radii in the lateral and vertical directions, respectively; f_f and f_r are the power fractions for the front and rear portions, respectively, which are taken to be 0.6 and 1.4, respectively.

To calculate the total power of the arc, as required in Eqs. (1) and (2), both current and voltage are needed. For the plasma WAAM process, the voltage is dependent on the current and cannot be directly specified using the equipment employed in Refs. [32, 33]. The following empirical voltage–current relation [36] was adopted in defining the heat source, viz.,

$$U = 10.80566 + 0.04816C \tag{3}$$

where U is the voltage and C is the current. Then the power can be obtained as the product of the voltage and current.

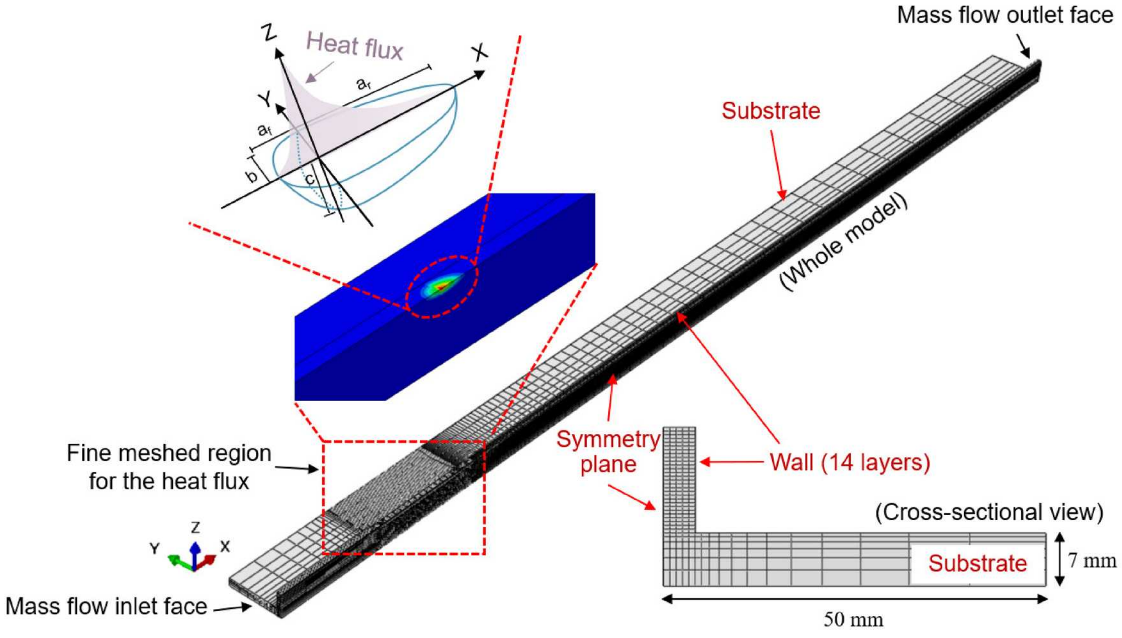

Figure 1. Steady-state thermal FEA model setup (only half part is considered due to symmetry).

2.2. Heat source model calibration

To determine the empirical parameters in the heat source model, a calibration was performed, and the predicted isothermal lines were compared with those derived from the metallurgical boundaries observed in the macrograph of the WAAM wall. In the heat source model, an arc efficiency value of 0.5 was adopted. Regarding the heat source shape parameters, the lateral and vertical radii were correlated with the layer width and height respectively, which were taken to be 50% the layer width and 110% the layer height. By contrast, the longitudinal radius was constant for different samples, i.e. 5 mm for the front region and 11 mm for the rear region. One WAAM sample was used to verify the efficacy of these assumed parameters for representing the actual plasma arc heat source. The process parameters and wall geometry are given in Table 2.

Figure 2 shows the comparison between the numerical prediction and experimental observation. In the macrograph, due to the thermal cycles caused by the multilayer deposition, the fusion boundary for each layer is barely discernible, but the banding microstructure associated with the β phase transformation and coarsening of α is clearly seen. The boundary of each band indicates the β-transus temperature (i.e. 1000°C) [8, 37]. It is evident that the predicted β-transus isothermal lines are consistent with the microstructural banding boundaries, especially for the top layer. However, some discrepancy is also observed for different layers, which can be largely attributed to the idealisation of the model, i.e. the model assumes that the layer geometry and deposition is perfectly symmetric and repeatable, while in reality there was some variation of the geometry and deposition from layer to layer, which was commonly seen in practice due to random errors (e.g. unstable equipment and environment).

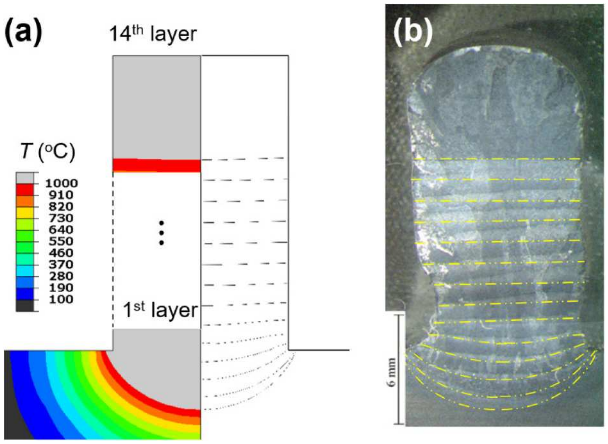

Figure 2. Comparison between FEA prediction and experimental observation: (a) predicted temperature distribution and isotherms (grey dashed) corresponding to the β-transus temperature; (b) macrograph of the observed microstructure bands superimposed with the predicted isotherms (yellow dashed) for β-transus temperature [32]. Note that the isotherms (dashed grey lines) predicted by the FEA model are mirrored to draw the isotherms (dashed yellow lines) superimposed in the macrograph of the full sample.

2.3. FEA model results

2.3.1. Temperature field

Typical results for the FEA model of the WAAM sample described in Section 2.2 are presented here. The predicted characteristics of the thermal variables for other WAAM samples are qualitatively similar, despite the difference in quantity due to a wide range of process parameters considered. Figure 3 shows the distribution and history of the temperature in the mid-width symmetry plane. For the steady-state thermal model employed here, the temperature history was obtained from the temperature distribution along the arc travel direction (i.e. X direction), through converting the distance to time ($t = \frac{s}{v}$, where s is the distance from the inlet face and v is the arc travel speed which is equal to the material flow speed in the model). The melt pool is indicated by the isotherm corresponding to the melting temperature of Ti-6Al-4V, which is taken to be 1640°C. The melt pool size (i.e. pool length and depth, Figure 4(a)) increased with more layers deposited until stabilised after the deposition of the 8th layer. This is because the interlayer temperature was set to be identical (100 °C) and the heat sink effect caused by the substrate was reduced when the wall height increased. To represent the steady state of the WAAM process, only the thermal variables for the 14th layer are analysed in following sections. The analysis focuses on two lines in the symmetry plane, one line located on the top of the 14th layer (i.e. 'layer top') and the other line with the same Z coordinate as the bottom point of the melt pool or fusion zone (i.e. 'fusion bottom').

Table 2. Parameters of the modelled WAAM process and wall geometry.

WFS (mm/s)	TS (mm/s)	C (Amp)	Wall width (mm)	Layer height (mm)
56.7	8.0	180.0	8.25	0. 99

2.3.2. Cooling rate

The variation rate of the temperature field is defined as follows

$$\dot{T} = \frac{\partial T}{\partial t} \tag{4}$$

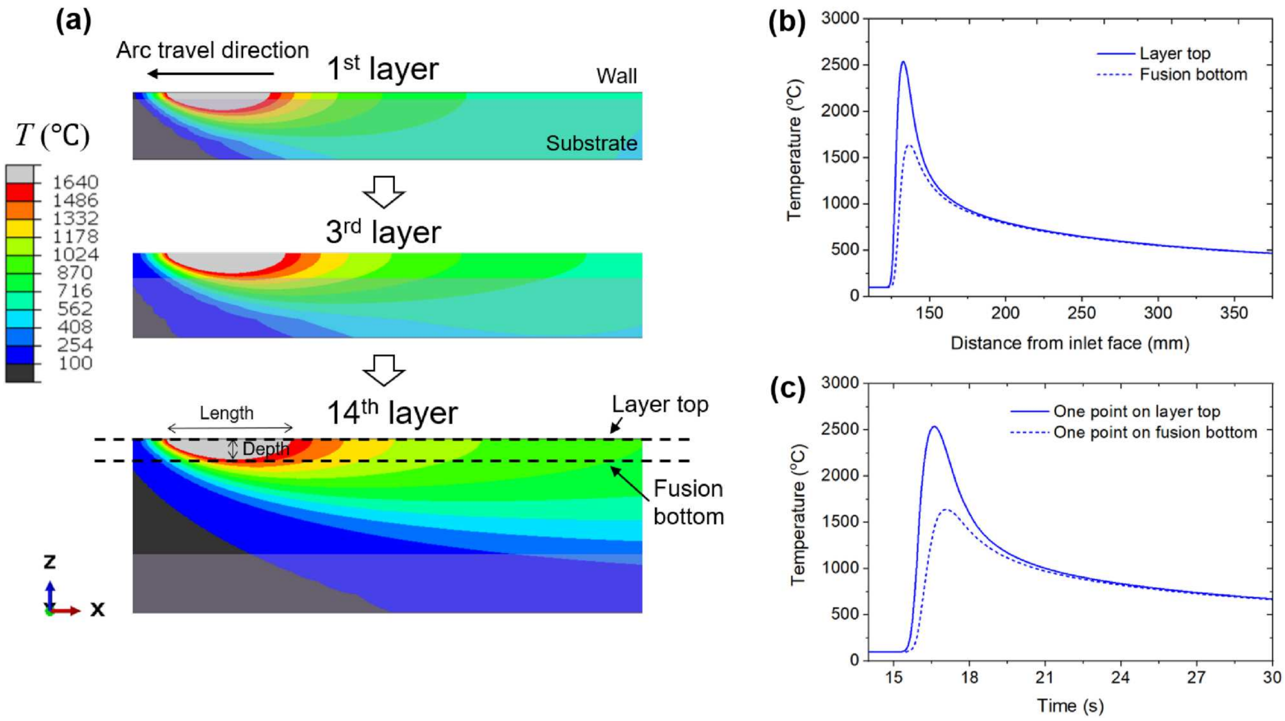

Figure 3. The predicted temperature distribution and history in the mid-width symmetry plane: (a) sectional distribution of the temperature predicted by the FEA model (shaded region indicates substrate); (b) distributions of temperature for the 14th layer (line paths are shown in a); (c) temperature histories at two arbitrary points on the lines of layer top and fusion bottom for the 14th layer (due to the steady thermal state modelled here, any points with same Z coordinate in the symmetry plane experienced identical thermal cycle after offsetting the time).

where T is the temperature and t is the time. Negative value of this derivative means cooling.

Figure 4 shows the predicted temperature variation rate in the symmetry plane. The molten region is excluded in the analysis since the accuracy of the FEA model is reliable mainly for the temperatures outside the melt pool, while the prediction accuracy is uncertain for the temperatures within the melt pool [38]. Here the cooling region, where the temperature variation rate is negative, is focused on for analysis due to the significance of the cooling rate on the microstructure formation. From the contour map (Figure 4(a)) the cooling region is dominant in the upper half of the wall behind the melt pool, and the cooling rate is nonuniformly distributed. Overall, the cooling rate is higher near the layer top than near the fusion bottom.

Figure 4(b) shows the dependence of the cooling rate on temperature at different locations on the layer top and fusion bottom (Figure 4(a), fusion depth = 2.5 mm). It is interesting to see that for temperatures below 1200°C the cooling rate is identical at any given temperature, whether the inspection location is on the layer top or fusion bottom, meaning that the nonuniform cooling rate shown in Figure 4(a) mainly arises from the nonuniformity of the temperature field (Figure 4(a)). It is also found that for a given temperature, the cooling rate is similar within the deposited layer height of 0.99 mm, and hence the average cooling rate within the 14th layer at each temperature will be used in the following analysis. There is a general trend that the cooling rate increases with temperature, except when the temperature is close to the melting point on the fusion bottom. Such an exception occurs because the melting temperature is the maximum temperature on the fusion bottom, at which the derivative of the temperature with time must be zero.

Although many finite element simulations of WAAM process are reported in the literature, few provides detailed analysis of the dependence of cooling rate on temperature and location. Specifically for plasma WAAM deposition of Ti-6Al-4V, we could not find FEA data from the literature for comparison of predicted cooling rates at different temperatures. Nevertheless, Xian et al. [39] reported that the cooling rate in the solidification temperature range (1600–1660°C) for gas tungsten arc WAAM deposition of Ti-6Al-4V ranges from 201 $^{\circ}C/s$ to 429 $^{\circ}C/s$, depending on the heat input. Our study shows that the cooling rate at 1600°C ranges from 243 $^{\circ}C/s$ to 518 $^{\circ}C/s$ for the plasma arc process, depending on the distance from the fusion

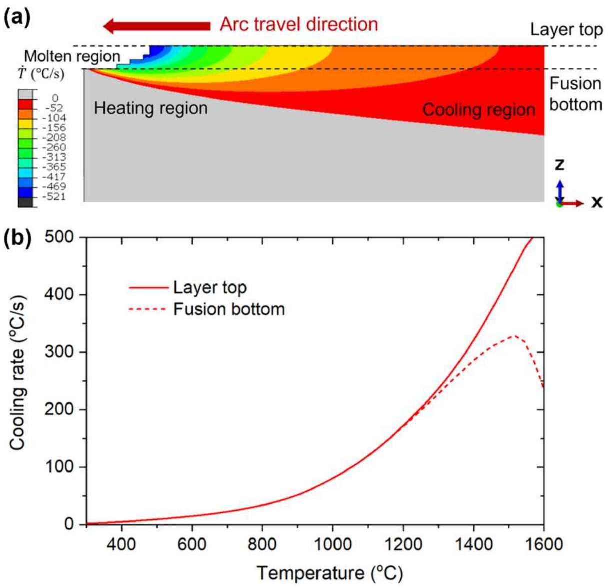

Figure 4. The predicted temperature variation rate in the symmetry plane: (a) sectional distribution of temperature variation rate obtained using the FEA model (the region near the melt pool is focused); (b) dependence of cooling rate on temperature for the layer top and fusion bottom (data are plotted only for the cooling region).

bottom. The difference in the predicted cooling rate could be attributed to the process difference between the plasma arc deposition and gas tungsten arc deposition, which are two WAAM variants.

2.3.3. Temperature gradient

The temperature gradient is expressed as follows

$$|\nabla T| = \sqrt{\left(\frac{\partial T}{\partial x}\right)^2 + \left(\frac{\partial T}{\partial y}\right)^2 + \left(\frac{\partial T}{\partial z}\right)^2} \quad (5)$$

It is difficult to calculate the temperature gradient through directly calculating the partial derivatives of the temperature in the deposited wall. We follow an indirect approach based on the Fourier's law, as demonstrated by Wang et al. [40].

Figure 5 shows the temperature gradient in the symmetry plane. A large temperature gradient is concentrated underneath the melt pool (Figure 5(a)). Only the temperature gradient in the cooling region is further analysed due to its major impact on the development of microstructure and hence mechanical properties. Unlike the cooling rate (Figure 4(b)), the temperature gradient is sensitive to both location and temperature, thus the layer top and fusion bottom are distinguished in the following analysis of temperature gradient. From Figure 5(b), it is clearly seen that for a given temperature, the temperature gradient on the fusion bottom is larger than that on the layer top. This is because on the fusion bottom there is stronger heat dissipation towards the relatively cool material below the melt pool.

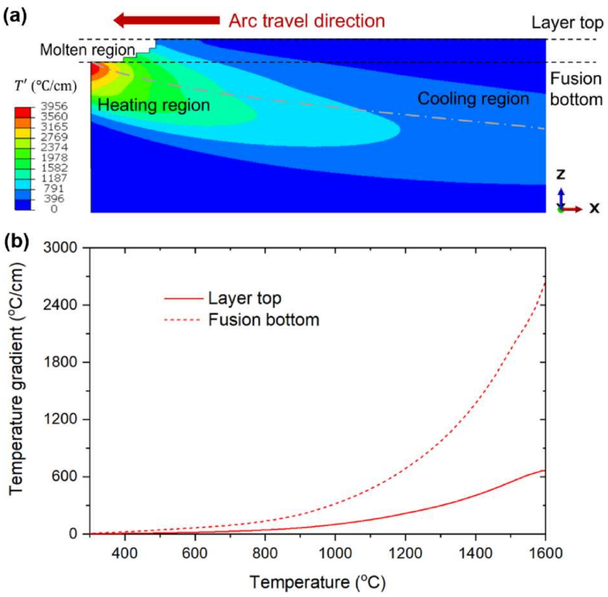

Figure 5. The predicted temperature gradient in the symmetry plane: (a) sectional distribution of temperature gradient obtained using the FEA model (the region near the melt pool is focused); (b) dependence of temperature gradient on temperature for the layer top and fusion bottom (data are plotted only for the cooling region).

Similar to the cooling rate, there is few data available in the literature for detailed analysis of the temperature gradient depending on both location and temperature. Xian et al. [39] reported that the temperature gradient along the building direction is approximately 3000°C/cm at the fusion bottom for the gas tungsten arc deposition of Ti-6Al-4V, which is similar to the result obtained here (Figure 5(b)) for the plasma arc deposition.

3. Knowledge-based bidirectional ML modelling

3.1. Data description and correlation coefficients

For ML modelling, the data from two feature categories was collected, i.e. process parameter feature, and thermal variable feature. The full details of data description are shown in Table 3. Three independent parameters for the plasma WAAM process are applied in this research, which are wire feed speed (WFS), arc current (C), and travel speed (TS). Three classes of thermal variables are considered and collected from the FEA models for the 26 samples, i.e. cooling rate, temperature gradient, and melt pool size, which have been defined in Section 2.3. Two types of cooling rates are considered in this research, the cooling rate at a

Table 3. Data description of WAAM process parameters and thermal variables.

Category	Type	Feature name	Description
Process parameter	Wire feed speed	WFS	Speed of supply material feeding, measured in *mm/s*
	Current	C	Current of arc power source, measured in *Amp*
	Travel speed	TS	Speed of arc torch, measured in *mm/s*
Thermal variable	Cooling rate	CR1300	Cooling rate at 1300°C, measured in *°C/s*
		CR1000	Cooling rate at 1000°C, measured in *°C/s*
		CR700	Cooling rate at 700°C, measured in *°C/s*
		CR1300_1000	Cooling rate from 1300°C to 1000°C in average, measured in *°C/s*
		CR1000_700	Cooling rate from 1000°C to 700°C in average, measured in *°C/s*
	Temperature gradient	TGT1300	Temperature gradient at 1300°C on layer top, measured in *°C/cm*
		TGT1000	Temperature gradient at 1000°C on layer top, measured in *°C/cm*
		TGT700	Temperature gradient at 700°C on layer top, measured in *°C/cm*
		TGB1300	Temperature gradient at 1300°C on fusion bottom, measured in *°C/cm*
		TGB1000	Temperature gradient at 1000°C on fusion bottom, measured in *°C/cm*
		TGB700	Temperature gradient at 700°C on fusion bottom, measured in *°C/cm*
	Melt pool size	D	Depth of melt pool, measured in *mm*
		L	Length of melt pool, measured in *mm*

specific temperature point and the average cooling rate between two special temperature points. Three special temperature points are selected in this study for evaluating the cooling rate and temperature gradient, which are 1300°C, 1000°C, and 700°C. The 1000°C is the characteristic temperature for β transformation of Ti-6Al-4V [37]. The 1300°C was selected as a characteristic temperature between the melting temperature and β-transus temperature, whilst the 700°C is representative of the martensitic transformation [41]. Based on these three special temperature points, data of seven cooling rates was extracted. Also, at each of these three temperature points, the temperature gradients on layer top and fusion bottom (Figure 5(a)) were collected for analysis. The depth and length of the predicted molten region are used to describe the melt pool size, while the melt pool width was equal to layer width and measured during the experiment (Appendix A). In total, 13 features were collected for describing the thermal behaviour.

The WFS, TS, and C are three basic input parameters of a plasma WAAM process. The thermal variables are the key process attributes that determine the quality of the deposited wall. To quantify the correlation between each feature, the Pearson Correlation Coefficient ($p_{X,Y}$) is employed (Table 4), which is a typical numerical measure of the strength of the linear relationship between two features (X and Y) and calculated using the following equation.

$$p_{X,Y} = \frac{Cov(X, Y)}{\sigma_X \sigma_Y} \tag{6}$$

In Eq. (6), $Cov(X, Y)$ is the covariance between two features, σ_X is the standard deviation of one feature and σ_Y is the standard deviation of another feature. The value of this coefficient is between -1 to $+1$, where the ± 1 represents the strongest linear relationship, and 0 indicates the weakest relationship [42]. In general, when the correlation coefficient is between $+0.3$ and -0.3, the two features have a weak relationship. When this coefficient is between $+0.3$ and $+0.8$ or -0.8 and -0.3, the indicated features are reasonably correlated. When it is larger than $+0.8$ or less than -0.8, there is a strong correlation between the two features [43].

For the features considered here, Table 4 displays that the cooling rate has a strong positive relationship with the travel speed, which has also been found in Ref. [40]. The arc current mainly affects the melt pool size and the top temperature gradient. Interestingly, the top and bottom temperature gradients exhibit different correlations to process parameters; specifically, to WFS, the coefficient is -0.69 for the top temperature gradient, but 0.069 for the bottom temperature gradient. The travel speed also has an opposite correlation to the top (-0.54) and bottom (0.77) temperature gradients.

Table 4. Correlation coefficients between process parameters and thermal variables.

Features	WFS	TS	C
Cooling rate	−0.087	0.66	−0.32
Melt pool depth	0.35	−0.21	0.76
Melt pool length	0.56	0.43	0.96
Top temperature gradient	−0.69	−0.54	−0.91
Bottom temperature gradient	0.069	0.77	0.02

3.2. Thermal deposition related knowledge

The spatial and temporal allocation of input energy results in different thermal profiles and solidification conditions, which determine the bead geometry, defect formation, microstructure evolution, and material properties [38, 44]. Energy related factors are important factors affecting the thermal variables. Two indices of energy input are considered in this research, i.e. linear heat input (Q_{linear}) and volumetric energy density ($D_{volumetric}$), which describe the energy input to the filler wire and substrate for melting the wire and generating the melt pool. The linear heat input is calculated as follows.

$$Q_{linear} = \frac{C^*U}{TS} \tag{7}$$

, TS is the travel speed, C is the current, and U is the voltage. The volumetric energy density ($D_{\text{volumetric}}$) is expressed as,

$$D_{\text{volumetric}} = \frac{C^*U}{WFS^*A_{wire}} \tag{8}$$

, WFS is the wire feed speed, and A_{wire} is the cross-sectional area of the wire, as defined below.

$$A_{wire} = \pi^* r_{wire}^2 \tag{9}$$

where r_{wire} is the radius of the wire.

Another process factor that affects the thermal variables is the cross-sectional area of the deposited layer (S), which represents the material input, calculated using the formula below:

$$S = \frac{WFS^*A_{wire}}{\text{TS}} \tag{10}$$

The correlation coefficients between the features associated with the energy input, material input, and thermal variables are shown in Table 5. Both linear heat input and deposited layer area have a stronger correlation to the cooling rate than the volumetric energy density. This is especially the case for linear heat input which has a correlation coefficient less than –0.8. The correlation coefficient between the deposited layer area and cooling rate is also very high at –0.71. It is interesting to see that the correlation coefficient between volumetric energy density and bottom temperature gradient is lower than 0.1, which indicates a weak correlation. But volumetric energy density has shown a stronger correlation with the top temperature gradient, −0.13, and the melt pool depth, 0.46.

Table 5. Correlation coefficients between process factors and thermal variables.

Features	Linear heat input	Volumetric energy density	Deposited layer area
Cooling rate	−0.84	−0.28	−0.71
Melt pool depth	0.73	0.46	0.45
Melt pool length	0.17	0.36	−0.093
Top temperature gradient	−0.049	−0.13	0.058
Bottom temperature gradient	−0.79	−0.098	−0.74

3.3. Knowledge-based bidirectional ML modelling for thermal variables

Our proposed bidirectional modelling approach consists of forward and backward prediction models. Three process factors were applied to embed the process knowledge in the ML model for forward and backward predictions. Initially, four different ML algorithms [45] were used for the modelling tasks: artificial neural network (ANN), linear regression, decision tree, and random forest. The ANN was implemented as the main ML modelling algorithm due to its superior prediction performance. The performance comparison between different ML models is shown in Appendices B–D. In this research, the ANNs were implemented using Python with the Keras library [46]. The Adam optimisation algorithm was used as the gradient descent optimiser with various learning rates. The general ANN structure is shown in Figure 6.

Both forward and backward models included three different neural networks for three predictions, with the details of each neural network varying in terms of input and output layers, learning rates, and the number of fully connected layers. The details of specific neural networks are described in the following sections.

3.3.1. Forward modelling

The structure of the forward modelling is shown in Figure 7. The basic process parameters, i.e. wire feed speed, travel speed and current, are the initial inputs, and the thermal variables are targets. Before applying the input data into the neural networks, the knowledge-based process factors, i.e. linear heat input, volumetric energy density, and deposited layer area, were calculated and incorporated with basic process

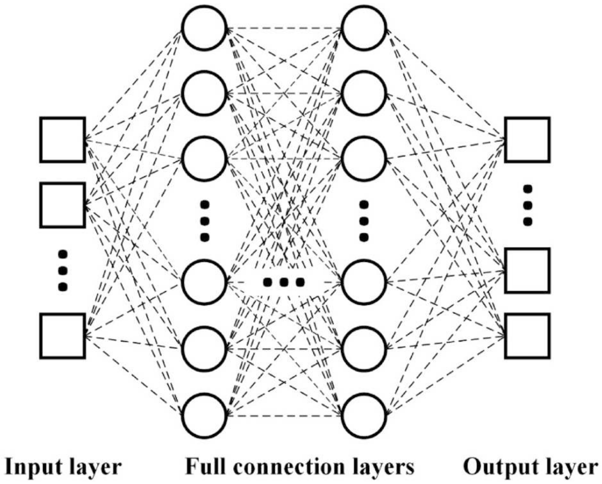

Figure 6. General artificial neural network structure.

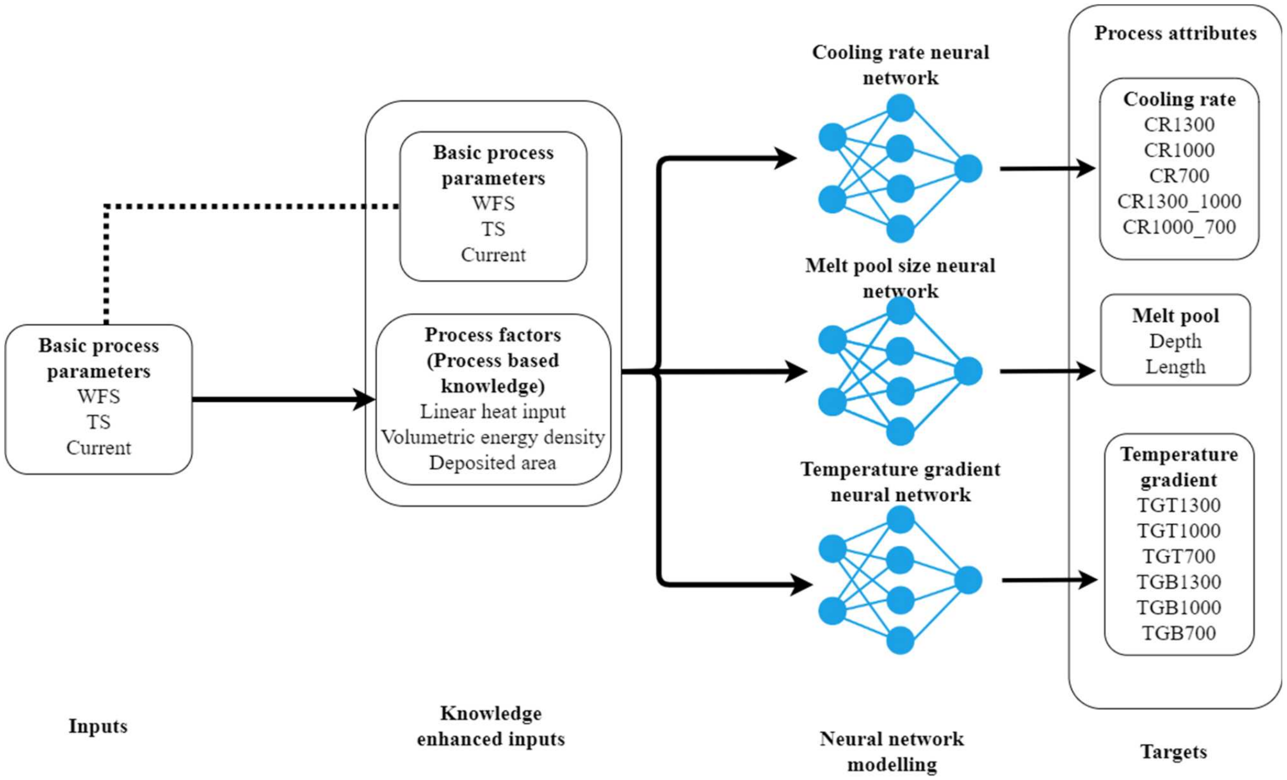

Figure 7. Forward process knowledge-based ML modelling for thermal variable prediction.

parameters as the enhanced inputs. The neural networks were built in the forward modelling, including cooling rate neural network, melt pool size neural network, and temperature gradient neural network. Each neural network was crafted to optimise its structure, focusing on variables such as learning rates, the number of fully connected layers, and neurons. The cooling rate neural network features a configuration of layers arranged in a 100-100-100-80-60 sequence, operating at a learning rate of 0.1. Similarly, the melt pool size neural network is constructed with a uniform layer sequence of 100-100-100-100-100, paired with a learning rate of 0.12. Lastly, the temperature gradient neural network is designed with a streamlined layer configuration of 100-100-80-60, also utilising a learning rate of 0.12.

3.3.2. Backward modelling

In the backward model (Figure 8), the basic process parameters are the targets, while the thermal variables are the inputs. Firstly, the process factors are predicted by the corresponding neural networks. Then the basic process parameters are calculated from the relationship between the process parameters and process factors based on the equations in Section 3.2. It should be noted that the deposition rate ($R_{deposition}$), expressed in Eq. (11), is usually pre-defined by the part building time requirement and determined by the wire feed speed. Therefore, the wire feed speed can be directly obtained from the required deposition rate which is considered as a known parameter in this research. Regarding the structure of each neural network, the linear heat input neural network comprises an 80-80-60-30 sequence with a learning rate of 0.2. The volumetric energy density network is constructed with a layer sequence of 100-100-100-80, paired with a learning rate of 0.18. Finally, the deposited area neural network's fully connected layers follow a 100-100-80-40 structure with a learning rate of 0.1.

$$R_{deposition} = WFS\,^{*}A^{*}_{wire}\;\rho \tag{11}$$

where ρ is the material density.

3.4. ML modelling results

To quantify the performance of the proposed modelling approach, two metrics, Root Mean Square Error (RMSE) and Pearson Correlation Coefficient (PCC), were used for the evaluation. Also, five-fold cross-validation method was employed for fully testing the prediction of the entire dataset [47]. The results obtained from the proposed approach, based on ANN, were also compared to three other ML algorithms, i.e. linear regression, decision tree, and random forest. The comparison between the ANN and other three ML algorithms is

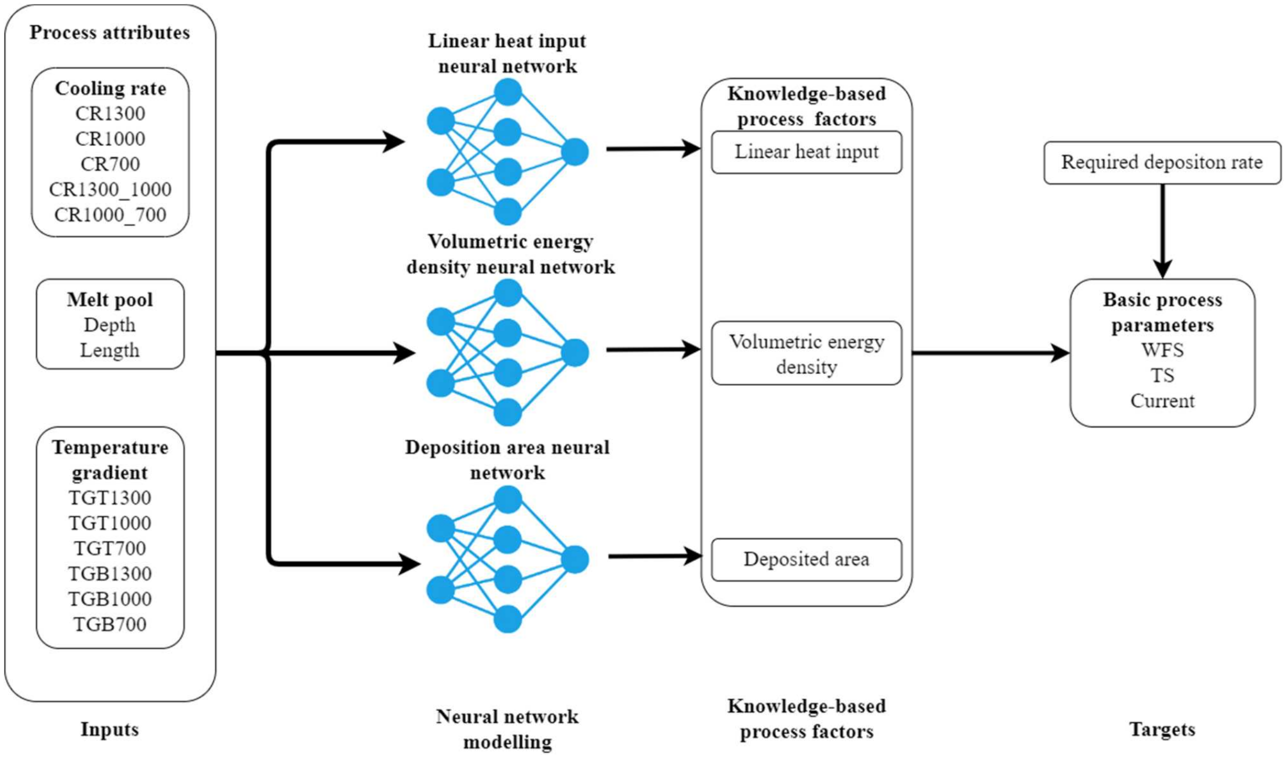

Figure 8. Backward process knowledge-based ML modelling for process parameter prediction.

shown in Appendices B–D. To determine the benefits of incorporating process knowledge, the results are compared with the models that did not involve the knowledge-based process factors (referred to as direct data-based predictions). The inverse analysis for predicting these process factors is also presented.

3.4.1. Metrics for evaluating results

RMSE and PCC were used as two evaluation metrics, which are expressed in Eqs. (12) and (13), respectively.

$$\boldsymbol{RMSE} = \sqrt{\frac{\sum_{i=1}^{n}(\boldsymbol{p}_{1,i} - \boldsymbol{a}_{1,i})^2}{\boldsymbol{n}}} \tag{12}$$

$$\boldsymbol{PCC} = \frac{\sum_i(\boldsymbol{p}_i - \bar{\boldsymbol{p}})(\boldsymbol{a}_i - \bar{\boldsymbol{a}})}{\sqrt{\sum_i(\boldsymbol{p}_i - \bar{\boldsymbol{p}})^2 \sum_i(\boldsymbol{a}_i - \bar{\boldsymbol{a}})^2}}, \tag{13}$$

In the above equations, p_i is the prediction data, $\bar{p}$ is the average value of the prediction data, a_i is the actual data and $\bar{a}$ is the average value of the entire data.

3.4.2. Thermal variable prediction results by forward models

The forward models predict three distinct types of process attributes, as outlined in Section 3.3.1. These include cooling rates at specified temperatures, 1300°C, 1000°C, and 700°C, as well as between these temperature ranges: 1300°C to 1000°C, and 1000°C to 700°C. The models also predict temperature gradients on the layer top and fusion bottom lines for the same set of temperatures, along with melt pool depth and length. Figure 9(a) and (b) display the average results for cooling rates and temperature gradients respectively, while Figure 9(c) shows the average result for melt pool depth and length. In general, the proposed process knowledge-based model achieved superior accuracy, as evidenced by low RMSE values and high PCC scores. For cooling rate prediction, the average RMSE is 7.263 °C/s, which is 12.9% lower than the predictions made without considering process factors, i.e. 8.342 °C/s; the PCC score is 0.935. The temperature gradients predicted using process factors achieved a PCC accuracy of 0.954 and an RMSE of 42.460 °C/cm, outperforming the direct predictions. Similarly, melt pool size predictions also demonstrated reasonably good performance, with a PCC of 0.944 and an RMSE of 0.82 mm.

3.4.3. Process parameter prediction results by backward model

In the case of the backward model, the primary focus is on two plasma WAAM process parameters: current and travel speed. Wire feed speed is typically pre-set by operators to meet the deposition rate requirement. Figure 10 illustrates the predicted values for current (Figure 10(a)) and travel speed (Figure 10(b)). Similar to the accuracy achieved in the forward modelling, the proposed

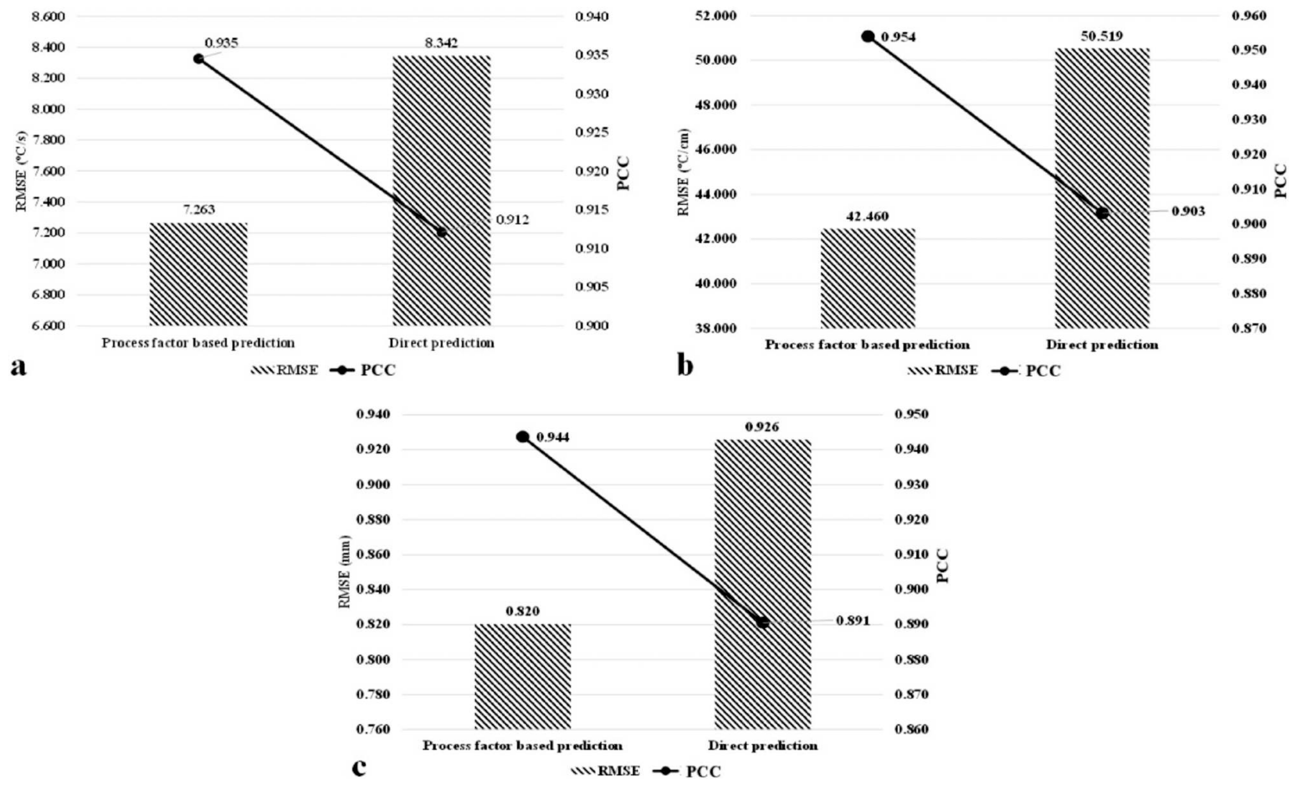

Figure 9. Thermal variable prediction accuracy by forward models: (a) cooling rate, (b) temperature gradient, (c) melt pool size.

backward model also delivers reliable prediction performance for both current and travel speed. As shown in Figure 10(a), the accuracy for current prediction reached a PCC of 0.945 and a RMSE of 12.176 *Amp*. Compared to the direct prediction method, this represents a decrement of approximately 40.56% in RMSE and an increment of 1.1% in PCC. For travel speed, the decrease in RMSE is 67.3% and the increase in PCC is 17%.

3.4.4. Additional validation and demonstration

To validate and demonstrate the accuracy and generality of the proposed approach, an additional experiment of a single pass Ti-6Al-4V wall deposition was carried out using the similar plasma WAAM process but a different deposition system. Regarding material setup, a substrate with dimensions of 250 mm × 60 mm × 7.3 mm and a filler wire with a diameter of 1.2 mm were used. The deposition process consisted of 10 layers, each layer deposited with a wire feed speed of 2.2 m/min and a current of 180 A. Variable travel speeds for the torch were applied: the first two layers were deposited at speeds of 4 and 4.5 mm/s, respectively, followed by a constant travel speed of 5 mm/s for the subsequent layers. The slower travel speed for the first two layers was helpful for counteracting the higher heat dissipation near the substrate. The average layer height and width

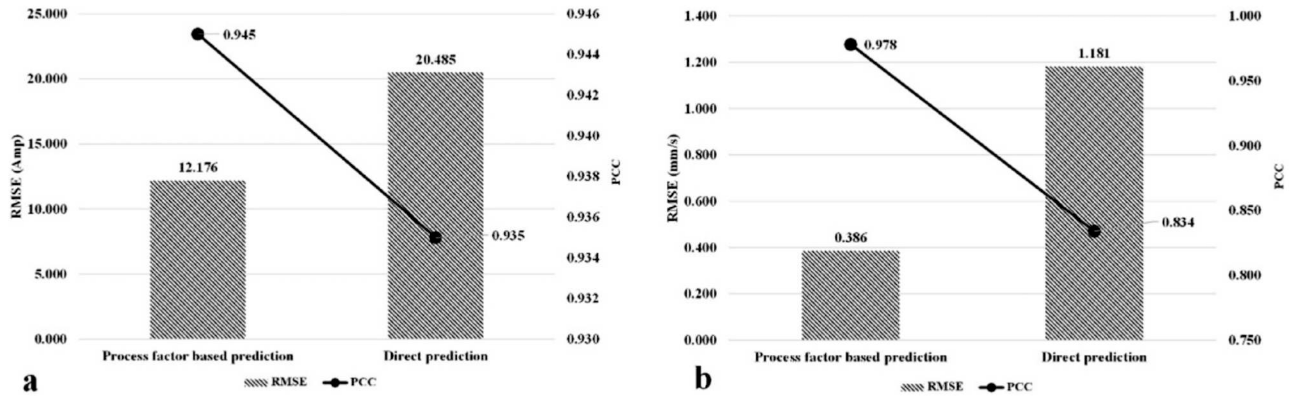

Figure 10. Process parameter prediction accuracy by backward models: (a) current, (b) travel speed.

were measured to be 0.98 and 9.23 mm, respectively. The plasma arc was generated using an EWM power source, with pure argon as both the plasma gas and shielding gas. The flow rates for the plasma gas and shielding gas were set at 0.8 and 8 L/min, respectively. Additionally, a local shielding device was incorporated, providing a gas flow rate of 68 L/min with pure argon as well. The experimental setup and deposited sample are depicted in Figure 11. During deposition, the plasma torch nozzle maintained a fixed distance of 8 mm from the substrate, and the wire feeder was inclined at an angle of 25° with respect to the travel direction. The substrate was securely held in place using six clamps to ensure stability. Controlled movement of the torch during deposition was facilitated by a 6-axis KUKA robot, which employed alternate travel directions to achieve uniform deposition.

The FEA modelling work, visualised in Figure 12, employed a steady state approach to analyse the thermal behaviour for the attributed sample. The steady state modelling approach in DED-AM involves analysing the thermal behaviour of the process under the assumption of a constant travel speed and a long deposition length. This approach focuses on the central region of the deposited layer, where thermal histories reach a steady state, providing a simplified yet accurate representation of the temperature field. By neglecting the varying thermal performance at the ends of the wall, the steady-state analysis delivers a static temperature distribution. More information on this modelling approach can be found in Section 2 and previous paper by Ding et al. [15].

The key thermal variables, including cooling rates and temperature gradients at various temperatures, as well as the melt pool sizes (i.e. length and depth), predicted by the FEA model for this new sample, are presented in Table 6. Additionally, Table 6 also provides the ML predicted thermal variables along with their respective errors and accuracies.

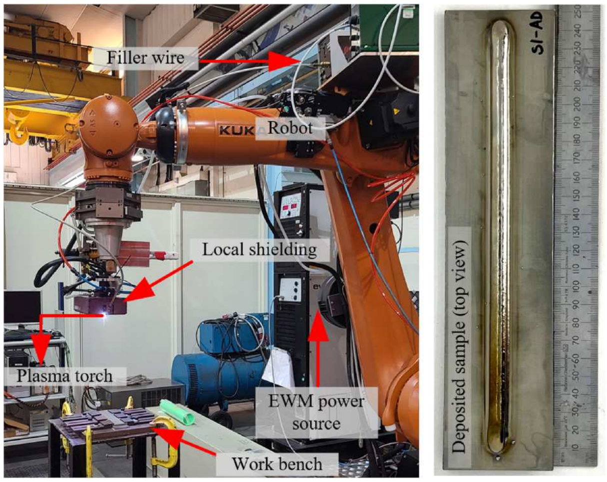

Figure 11. The experimental setup and deposited sample

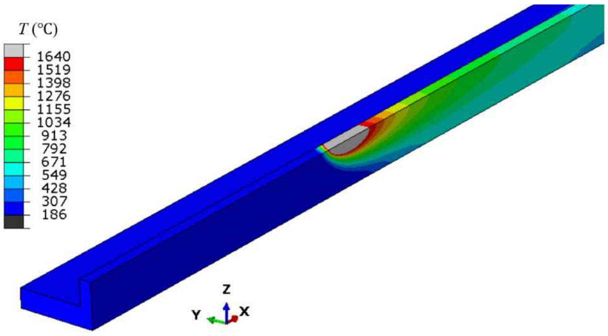

Figure 12. FEA model of the additional sample for further validation and demonstration

From Table 6, it is evident that accurate predictions are made for the cooling rate at 1300 °C (accuracy: 89.2%, error: 10.519 °C/s), the bottom temperature gradients at 1000 °C (accuracy: 92.9%, error: 19.724 °C/cm) and 700°C (accuracy: 92.8%, error: 6.341°C/cm), as well as the melt pool depth (accuracy: 90.3%, error: 0.416 mm). Overall, the proposed ML approach achieves around 75% accuracy in predicting cooling rates and temperature gradients, and over 80% accuracy for melt pool size. Since this additional validation experiment was conducted using a different plasma WAAM system, while previous experimental data for the ML model construction were obtained using an old system which is not available now [32, 33], the errors could be partially due to the difference in the specific systems and environments.

The predictions of the backward ML model are also compared with the additional validation experiment, as shown in Table 7. The accuracy of the predicted basic process parameters is notably high in this specific case, which is over 99% for the current and about 94% for the travel speed.

4. Discussion

4.1. Capability and advantages of the proposed modelling approach

According to the results shown in the case study based on the 26 samples, the proposed modelling approach can predict the thermal variables and basic process parameters using the bidirectional ML model with a low error (< 7%). Also, the computational time of the ML model is generally less than 100 ms, which is dramatically lower than the physics-based simulation tools, like FEA and CFD. Different from the recent research

Table 6. Thermal variable prediction results comparison.

Thermal variables		Results from FEA model	Results from ML approach	Error	Average error	Accuracy	Average accuracy
Cooling rate (°C/s)	CR1300	97.181	86.662	10.519	10.051	89.2%	76.1%
	CR1000	43.789	32.961	10.828		75.3%	
	CR700	13.503	10.018	3.485		74.2%	
	CR1300_1000	68.984	52.700	16.284		76.4%	
	CR1000_700	26.543	17.405	9.138		65.6%	
Temperature gradient (°C/cm)	TGT1300	197.000	131.843	65.157	45.874	66.9%	74.4%
	TGT1000	89.500	51.754	37.746		57.8%	
	TGT700	29.440	16.957	12.483		57.6%	
	TGB1300	610.000	743.791	133.791		78.1%	
	TGB1000	276.240	256.516	19.724		92.9%	
	TGB700	88.470	82.129	6.341		92.8%	
Melt pool size (mm)	D	4.282	4.698	0.416	2.481	90.3%	83.8%
	L	20.000	24.545	4.545		77.3%	

efforts using ML to predict the full-field transient temperatures [48], the case study of the proposed modelling framework selected key thermal variables for predictions. This treatment has two advantages at least. First, it is unfeasible for a process designer to provide full-field temperature as the process requirement but easy to define some key thermal variables for the backward model prediction. Second, when a DED-AM process reaches steady state, most material points along the heat source travel path experience identical thermal histories. Therefore, the prediction of steady-state thermal variables is more efficient and equally informative. It also represents an attempt to generate 'smart' data rather than big data for engineering ML models, which can reduce the computational burden for the model training and circumvent the associated data management issue [49]. As in the case study the thermal variables were examined as the process attributes, in principle, different combinations of process parameters could obtain similar thermal variables. So, it is physically less meaningful to predict the basic process parameters directly backward from performance requirements. By contrast, the relation between process factors and requirements is more fundamental. The physics-based process factors govern the energy and material inputs, which can be converted to basic process parameters for different DED-AM systems.

Another interesting finding is that the ML models were enhanced by incorporating the process knowledge in the proposed approach. The process factor-based models obtained better results compared to the direct data-based predictions, and in average the former are about 10% more accurate than the latter. Integrating the process knowledge and physics information becomes an effective strategy to improve data-driven technologies, such as ML algorithms. In this research, the relevant process factors were calculated and involved into the thermal modelling to enhance the predictive capability and accuracy.

Usually data-driven technologies need large data sets for training. Although only 26 experimental data sets were used for building the ML models, the parameter space is large, covering a wide range of currents, wire feed speeds and travel speeds (Appendix A). Similarly, the linear heat input, volumetric energy density and deposited layer area are also examined over a wide range. Remarkable performance has been achieved thanks to the incorporation of process knowledge in the ML models. If the training data set were larger, the accuracy of the predictions could be even higher. Many researchers have also tackled AM issues by using physics-informed ML algorithms [31,50], which have become increasingly important and popular in many fields especially for engineering problems. By comparing ANN with other ML algorithms, as shown in Appendices B and C, we demonstrate that the process factor-supported ANN can achieve better results than other ML models. It means that the ANN adapts to the new input features easier than the other ML algorithms, and ANN is less sensitive to the different targets.

Comparing to the most of current data-driven AM research, the proposed method includes double

Table 7. Process factor and basic process parameter prediction results comparison.

	Process factors			Basic process parameters	
	Linear heat input	Volumetric energy density	Deposited area	Current	Travel speed
Actual value	701.081 J/mm	84.757 J/mm^3	8.271 mm^2	180 Amp	5 mm/s
Predicted value	528.040 J/mm	88.617 J/mm^3	7.7962 mm^2	179.99 Amp	5.305 mm/s
Error	173.041 J/mm	3.86 J/mm^3	0.4748 mm^2	0.001 Amp	0.3048 mm/s
Accuracy	75.3%	95.4%	94.3%	99.9%	93.9%

directions for predictions, which are useful for different purposes. Especially, the backward modelling can help the process developers to rapidly determine the process parameters that are input to the AM system based on the performance requirement. It has built up a strong confidence and potential for a real-time online AM digital application. This application can significantly reduce the number of experiments and tests, which is one of the critical research and industrial issues in DED-AM. However, given the complexity of AM processes, potential uncertainty about the robustness of the approach is still open to research and more case studies are needed in future work.

4.2. Further consideration of the thermal analysis

One limitation of the case study could arise from the assumption that in the FEA model, an arc efficiency of 0.5 was adopted from heat source calibration, as it led to model predictions with best agreement with the calibration experiment. However, the arc efficiency could vary with process parameters and the typical value ranges from 0.49 to 0.66 for plasma arc welding [51]. To inspect the sensitivity of the results to the energy distribution, another arc efficiency of 0.65, and different shape parameters, i.e. $a_f = 2$ mm and $a_r = 6$ mm, were adopted to represent higher energy density distribution. Such changes led to larger melt pool sizes, lower cooling rates and smaller temperature gradients. Nevertheless, the ML prediction accuracy, which is of major interest here, is not sensitive to such changes, as shown in Appendices B–D, meaning that the conclusions about the ML performance still hold. In future work, the arc efficiency and shape parameters may need to be determined for each sample through serial experimental calibration, which, however, will significantly increase the data demand. It should be also mentioned that, in the case study, we focused on the thermal variables for the top layer of the wall, while additional analysis could be performed for the evolution of thermal variables during deposition of subsequent layers.

4.3. Generalised applications

The proposed ML modelling approach, for a case study, places emphasis on thermal variable modelling, combined with the application of FEA simulation, thereby enabling a comprehensive understanding and prediction of thermal behaviour in the DED-AM process. This knowledge-based bidirectional modelling approach also presents the potential for extension into various other digital applications pertinent to DED-AM, including CFD and analytical models. Figure 13 provides an overview of the generalised framework for knowledge-based bidirectional modelling in DED-AM.

Within this framework, as depicted in Figure 13, both the basic process parameters and the knowledge-based process factors serve as inputs and outputs for the ML models. These factors are crucial in enhancing the performance and efficiency of the ML models by incorporating domain-specific knowledge and insights. By integrating such knowledge-based factors into the modelling process, the ML models can better capture the complexities and intricacies inherent in the DED-AM process, thereby improving predictive accuracy and overall effectiveness. Furthermore, this expanded framework not only enhances the understanding of thermal variables but also provides a robust foundation for optimising various aspects of the DED-AM process and constructing a digital twin. Through the incorporation of knowledge-based factors, the ML models can adapt and evolve in response to changing process conditions, ultimately contributing to more efficient and effective AM practices.

5. Conclusions

A new bidirectional data-driven approach has been proved as a promising solution to DED-AM process research and industry issues. The proposed approach developed a generic method for bidirectional modelling which integrated physical and empirical relations and process knowledge. This approach combines data-driven and physics-based models, which is inspired by

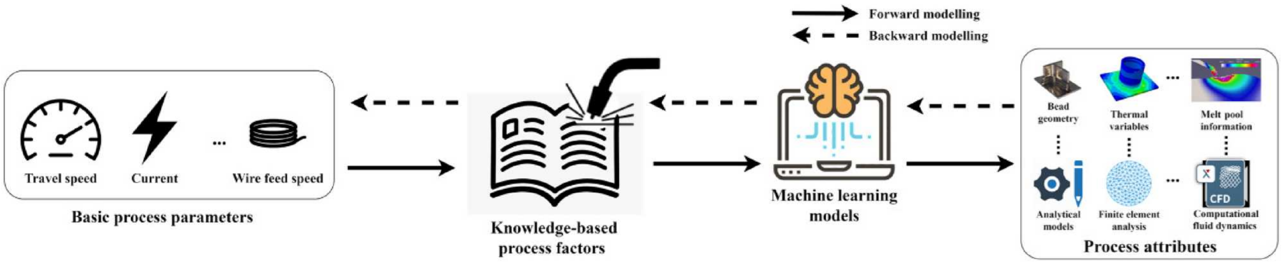

Figure 13. The generalised framework of knowledge-based bidirectional modelling.

a review of the state of the art. Some highlighted novelty and finding of this research are summarised as follows:

- The proposed approach has offered better insight due to the incorporation of process knowledge in data analytics. The inputs and outputs of the proposed modelling are obtained based on the understanding of the physical mechanisms, in which the fundamental relationship is naturally embedded. Thermal variables at characteristic temperatures are selected based on analysis of FEA results, as an attempt to generate smart data with reduced data size for ML model.
- Benefiting from the knowledge-based data-driven method, as compared to the direct prediction, the proposed approach is more effective with higher prediction accuracy for both directions of predictive modelling.
- The thermal attributes of plasma WAAM were revealed and correlated with process parameters and factors. The desired thermal variables can be achieved by using the predicted process inputs. Furthermore, the process factors can be adapted to different AM systems through a suitable parameter conversion.

Acknowledgement

The authors would like to thank Nisar Shah and Mark Allen for their technical support.

Disclosure statement

No potential conflict of interest was reported by the author(s).

Funding

The authors would like to express their gratitude to Engineering and Physical Sciences Research Council (EPSRC) (EP/R027218/1, New Wire Additive Manufacturing) for supporting aspects of this research.

Author contributions

Conceptualisation: Jian Qin and Yongle Sun; Methodology: Jian Qin, Yongle Sun, Pradeeptta Taraphdar and Shuo Feng; Investigation: Pradeeptta Taraphdar, James Wainwright, Wai Jun Lai, and Yongle Sun; Writing – original draft: Jian Qin, Yongle Sun and Pradeeptta Taraphdar; Writing – review & editing: James Wainwright, Wai Jun Lai, Jialuo Ding and Stewart Williams; Supervision: Jialuo Ding and Stewart Williams; Funding acquisition: Jialuo Ding and Stewart Williams.

Data availability statement

Data underlying this study can be accessed through the Cranfield University repository at [https://doi.org/10.17862/cranfield.rd.25308583].

References

[1] Gibson, Ian, David W Rosen, Brent Stucker, and Mahyar Khorasani. 2021. *Additive manufacturing technologies*. Vol. 17. Switzerland: Springer.

[2] Froes FH, Boyer R. *Additive manufacturing for the aerospace industry*. Netherlands: Elsevier; 2019.

[3] Gibson, Ian, David Rosen, and Brent Stucker. 2015. Directed energy deposition processes. In *Additive manufacturing technologies*, 245–268. New York: Springer.

[4] Ou W, Mukherjee T, Knapp GL, et al. Fusion zone geometries, cooling rates and solidification parameters during wire arc additive manufacturing. Int J Heat Mass Transf. 2018;127 (December):1084–1094. doi:10.1016/j.ijheatmasstransfer.2018.08.111

[5] Cunningham CR, Flynn JM, Shokrani A, et al. Invited review article: strategies and processes for high quality wire arc additive manufacturing. Addit Manuf. 2018;22:672–686. doi:10.1016/j.addma.2018.06.020

[6] Ge J, Ma T, Han W, et al. Thermal-induced microstructural evolution and defect distribution of wire-arc additive manufacturing 2Cr13 part: numerical simulation and experimental characterization. Appl Therm Eng. 2019;163 (December):114335. doi:10.1016/j.applthermaleng.2019.114335

[7] Wu Q, Mukherjee T, De A, et al. Residual stresses in wire-arc additive manufacturing – hierarchy of influential variables. Addit Manuf. 2020;35(October):101355. doi:10.1016/j.addma.2020.101355

[8] Ho A, Zhao H, Fellowes JW, et al. On the origin of microstructural banding in Ti-6Al4V wire-arc based high deposition rate additive manufacturing. Acta Mater. 2019;166 (March):306–323. doi:10.1016/j.actamat.2018.12.038

[9] Cheepu M, Kantumuchu VC. Numerical simulations of the effect of heat input on microstructural growth for MIG-based wire arc additive manufacturing of inconel 718. Trans Indian Inst Met. 2023;76(2):473–481. doi:10.1007/s12666-022-02749-5

[10] DebRoy T, Wei HL, Zuback JS, et al. Additive manufacturing of metallic components – process, structure and properties. Prog Mater Sci. 2018;92:112–224. doi:10.1016/j.pmatsci.2017.10.001

[11] Hu D, Kovacevic R. Sensing, modeling and control for laser-based additive manufacturing. Int J Mach Tools Manuf. 2003;43:51–60.

[12] Chergui A, Villeneuve F, Béraud N, et al. Thermal simulation of wire arc additive manufacturing: a new material deposition and heat input modelling. Int J Interact Des Manuf. 2022;16(1):227–237. doi:10.1007/s12008-021-00824-7

[13] Francois MM, Sun A, King WE, et al. Modeling of additive manufacturing processes for metals: challenges and opportunities. Cur Opin Solid State Mater Sci. 2017;21 (4):198–206. doi:10.1016/j.cossms.2016.12.001

[14] Yang Y, van Keulen F, Ayas C. A computationally efficient thermal model for selective laser melting. Addit Manuf.

2020;31(January):100955. doi:10.1016/j.addma.2019.100955

[15] Ding J, Colegrove P, Mehnen J, et al. Thermo-mechanical analysis of wire and arc additive layer manufacturing process on large multi-layer parts. Comput Mater Sci. 2011;50(12):3315–3322. doi:10.1016/j.commatsci.2011.06.023

[16] Liang X, Cheng L, Chen Q, et al. A modified method for estimating inherent strains from detailed process simulation for fast residual distortion prediction of single-walled structures fabricated by directed energy deposition. Addit Manuf. 2018;23(October):471–486. doi:10.1016/j.addma.2018.08.029

[17] Ding J, Colegrove P, Mehnen J, et al. A computationally efficient finite element model of wire and Arc additive manufacture. Int J Adv Manuf Technol. 2014;70(1–4):227–236. doi:10.1007/s00170-013-5261-x

[18] Martukanitz R, Michaleris P, Palmer T, et al. Toward an integrated computational system for describing the additive manufacturing process for metallic materials. Addit Manuf. 2014;1-4(October):52–63. doi:10.1016/j.addma.2014.09.002

[19] Li C, Fu CH, Guo YB, et al. A multiscale modeling approach for fast prediction of part distortion in selective laser melting. J Mater Process Technol. 2016;229(October):703–712. doi:10.1016/j.jmatprotec.2015.10.022

[20] Denlinger ER, Irwin J, Michaleris P. Thermomechanical modeling of additive manufacturing large parts. J Manuf Sci Eng Trans ASME. 2014;136(6):061007. doi:10.1115/1.4028669

[21] Bartsch K, Pettke A, Hübert A, et al. On the digital twin application and the role of artificial intelligence in additive manufacturing: a systematic review. J Phys: Mater. 2021;4:032005.

[22] Johnson NS, Vulimiri PS, To AC, et al. Invited review: machine learning for materials developments in metals additive manufacturing. Addit Manuf. 2020;36:101641. doi:10.1016/j.addma.2020.101641

[23] Zhu Q, Liu Z, Yan J. Machine learning for metal additive manufacturing: predicting temperature and melt pool fluid dynamics using physics-informed neural networks. Comput Mech. 2021;67(2):619–635. doi:10.1007/s00466-020-01952-9

[24] Pham TQD, Hoang TV, Pham QT, et al. (2021). Data-driven prediction of temperature evolution in metallic additive manufacturing process. ESAFORM 2021 - 24th International Conference on Material Forming. PoPuPS (University of LiFge Library). doi:10.25518/esaform21.2599

[25] Fetni S, Pham QDT, Tran VX, et al. (2021). Thermal field prediction in DED manufacturing process using artificial neural network. ESAFORM 2021 - 24th International Conference on Material Forming. PoPuPS (University of LiFge Library). doi:10.25518/esaform21.2812

[26] Roy M, Wodo O. Data-driven modeling of thermal history in additive manufacturing. Addit Manuf. 2020;32(March):101017. doi:10.1016/j.addma.2019.101017

[27] Haghighi M, Alireza JD, Sun Y, et al. Thermo-capillary-gravity bidirectional modelling for evaluation and design of wire-based directed energy deposition additive manufacturing. J Manuf Process. 2023;107(December):320–332. doi:10.1016/j.jmapro.2023.09.069

[28] Xiong J, Zhang G, Hu J, et al. Forecasting process parameters for GMAW-based rapid manufacturing using closed-loop iteration based on neural network. Int J Adv Manuf Technol. 2013;69(1):743–751. doi:10.1007/s00170-013-5038-2

[29] Ding D, He F, Yuan L, et al. The first step towards intelligent wire arc additive manufacturing: an automatic bead modelling system using machine learning through industrial information integration. J Ind Inf Integr. 2021;23(September):100218. doi:10.1016/j.jii.2021.100218

[30] Qin J, Hu F, Liu Y, et al. Research and application of machine learning for additive manufacturing. Addit Manuf. 2022;52(April):102691. doi:10.1016/j.addma.2022.102691

[31] Ko H, Witherell P, Lu Y, et al. Machine learning and knowledge graph based design rule construction for additive manufacturing. Addit Manuf. 2021;37(January):101620. doi:10.1016/j.addma.2020.101620

[32] Martina F. (2010). Study of the benefits of plasma deposition of Ti-6al-4v structures made by additive layer manufacture [MSc thesis]. Cranfield University.

[33] Martina F, Mehnen J, Williams SW, et al. Investigation of the benefits of plasma deposition for the additive layer manufacture of Ti–6Al–4V. J Mater Process Technol. 2012;212(6):1377–1386. doi:10.1016/j.jmatprotec.2012.02.002

[34] Goldak J, Chakravarti A, Bibby M. A new finite element model for welding heat sources. Metall Trans B. 1984;15(2):299–305. doi:10.1007/BF02667333

[35] Ding J. *Thermo-mechanical analysis of wire and arc additive manufacturing process.* Cranfield: Cranfield University; 2012.

[36] Bridgeman PJ. *Investigation of plasma transferred arc dynamic effects in wire + arc additive manufacturing.* Cranfield: Cranfield University; 2021.

[37] Tamirisakandala S, Bhat RB, Miracle DB, et al. Effect of boron on the beta transus of Ti–6Al–4V alloy. Scr Mater. 2005;53(2):217–222. doi:10.1016/j.scriptamat.2005.03.038

[38] Wei HL, Mukherjee T, Zhang W, et al. Mechanistic models for additive manufacturing of metallic components. Prog Mater Sci. 2021;116(February):100703. doi:10.1016/J.PMATSCI.2020.100703

[39] Xian G, Oh Jm, Lee J, et al. Effect of heat input on microstructure and mechanical property of wire-arc additive manufactured Ti-6Al-4V alloy. Weld World. 2022;66(5):847–861. doi:10.1007/s40194-021-01248-3

[40] Wang C, Sun Y, Chen G, et al. A simplified modelling approach for thermal behaviour analysis in hybrid plasma arc-laser additive manufacturing. Int J Heat Mass Transf. 2022;195(October):123157. doi:10.1016/j.ijheatmasstransfer.2022.123157

[41] Elmer JW, Palmer TA, Babu SS, et al. Phase transformation dynamics during welding of Ti–6Al–4V. J Appl Phys. 2004;95(12):8327–8339. doi:10.1063/1.1737476

[42] Charaniya S, Le H, Rangwala H, et al. Mining manufacturing data for discovery of high productivity process characteristics. J Biotechnol. 2010;147(3–4):186–197. doi:10.1016/j.jbiotec.2010.04.005

[43] Desai N, Dhameliya K, Desai V. Feature extraction and classification techniques for speech recognition: a review. Int J Emerg Technol Adv Eng. 2013;3(12):367–371.

[44] Oliveira JP, Santos TG, Miranda RM. Revisiting fundamental welding concepts to improve additive manufacturing: from theory to practice. Prog Mater Sci. 2020;107(January):100590. doi:10.1016/j.pmatsci.2019.100590

[45] Bonaccorso G. *Machine learning algorithms*. Birmingham: Packt Publishing Ltd; 2017.

[46] Gulli A, Pal S. *Deep learning with Keras*. Birmingham: Packt Publishing Ltd; 2017.

[47] Stone M. Cross-validatory choice and assessment of statistical predictions. J R Stat Soc Ser B: Stat Methodol. 1974;36 (2):111–133. doi:10.1111/j.2517-6161.1974.tb00994.x

[48] Ness KL, Paul A, Sun L, et al. Towards a generic physics-based machine learning model for geometry invariant thermal history prediction in additive manufacturing. J Mater Process Technol. 2022;302(April):117472. doi:10.1016/j.jmatprotec.2021.117472

[49] Chinesta F, Cueto E, Abisset-Chavanne E, et al. Virtual, digital and hybrid twins: a New paradigm in data-based engineering and engineered data. Arch Comput Methods Eng. 2020;27(1):105–134. doi:10.1007/s11831-018-9301-4

[50] Gaikwad A, Giera B, Guss GM, et al. Heterogeneous sensing and scientific machine learning for quality assurance in laser powder Bed fusion – a single-track study. Addit Manuf. 2020;36(December):101659. doi:10.1016/j.addma.2020.101659

[51] Evans DM, Huang D, McClure JC, et al. Arc efficiency of plasma arc welding. Weld J. 1998;77(2):53–58.

Appendices

Appendix A. Parameters of WAAM samples [32]

Sample	WFS [mm/s]	TS [mm/s]	Current [A]	Estimated voltage [V]	Linear heat input [J/mm]	Volumetric energy density [J/mm^3]	Deposited layer area [mm^2]	Average layer height [mm]	Average wall width [mm]
1	66.7	10.0	250.0	22.85	571	76	7.5	1.02	8.14
2	33.3	2.0	150.0	18.03	1352	72	18.8	1.36	14.71
3	40.0	8.0	202.2	20.54	519	92	5.7	0.66	8.03
4	86.7	4.8	197.8	20.33	838	41	20.4	2.1	10.60
5	40.8	4.0	215.6	21.19	1142	99	11.5	1.23	11.17
6	50.0	10.0	136.7	17.39	238	42	5.7	1.01	5.92
7	50.0	10.0	200.0	20.44	409	72	5.7	0.72	7.72
8	90.5	10.0	240.0	22.36	537	52	10.2	1.05	9.54
9	56.7	8.0	256.7	23.17	743	93	8.0	0.86	9.69
10	40.0	6.0	140.0	17.55	409	54	7.5	0.88	8.03
11	82.9	4.1	282.9	24.43	1686	74	22.9	1.4	16.44
12	20.0	2.0	120.0	16.58	995	88	11.3	0.94	12.17
13	80.8	6.5	250.6	22.87	882	63	14.1	1.26	11.70
14	40.0	2.0	120.0	16.58	995	44	22.6	2.04	11.61
15	20.0	4.0	120.0	16.58	498	88	5.7	0.67	8.41
16	100.0	7.0	300.0	25.25	1082	67	16.2	1.24	13.21
17	40.0	2.0	160.0	18.51	1481	65	22.6	1.52	15.82
18	65.7	6.6	190.0	19.96	574	51	11.3	1.24	9.26
19	100.0	10.0	300.0	25.25	758	67	11.3	1.15	9.88
20	68.6	3.4	200.0	20.44	1202	53	22.8	1.62	14.36
21	61.4	3.1	261.4	23.39	1973	88	22.4	1.19	16.60
22	70.3	10.0	190.0	19.96	379	48	8.0	1.12	7.34
23	76.1	8.0	240.0	22.36	671	62	10.8	1.11	9.79
24	50.0	10.0	250.0	22.85	571	101	5.7	0.72	8.28
25	56.7	8.0	180.0	19.47	438	55	8.0	0.99	8.25
26	20.0	4.0	220.0	21.40	1177	208	5.7	0.69	10.70

Appendix B. Forward prediction results based on an arc efficiency of 0.65

		RMSE		PCC	
Targets	ML algorithms	Process factor based prediction	Direct prediction	Process factor based prediction	Direct prediction
Cooling rate	Neural network	7.263°C/s	8.342°C/s	0.935	0.912
	Linear regression	11.364°C/s	11.983°C/s	0.788	0.768
	Decision tree	10.402°C/s	18.172°C/s	0.865	0.728
	Random forest	8.643°C/s	14.530°C/s	0.882	0.769
Melt pool size	Neural network	0.820 mm	0.926 mm	0.944	0.891
	Linear regression	1.510 mm	2.115 mm	0.943	0.884
	Decision tree	2.559 mm	1.855 mm	0.831	0.877
	Random forest	1.891 mm	1.982 mm	0.907	0.892
Temperature gradient	Neural network	42.460°C/cm	50.519°C/cm	0.954	0.903
	Linear regression	30.411°C/cm	31.349°C/cm	0.933	0.839
	Decision tree	55.924°C/cm	65.454°C/cm	0.883	0.818
	Random forest	37.227°C/cm	40.487°C/cm	0.930	0.892

Appendix C. Backward prediction results based on an arc efficiency of 0.65

		RMSE		PCC	
Targets	ML algorithms	Process factor based prediction	Direct prediction	Process factor based prediction	Direct prediction
Current	Neural network	12.176 Amp	20.485 Amp	0.945	0.935
	Linear regression	23.878 Amp	85.074 Amp	0.805	0.584
	Decision tree	24.835 Amp	62.203 Amp	0.606	0.587
	Random forest	18.906 Amp	59.018 Amp	0.827	0.699
TS	Neural network	0.386 mm/s	1.181 mm/s	0.978	0.834
	Linear regression	0.897 mm/s	1.934 mm/s	0.897	0.860
	Decision tree	1.848 mm/s	2.082 mm/s	0.679	0.638
	Random forest	1.396 mm/s	1.445 mm/s	0.764	0.754

Appendix D. Process knowledge relevant features prediction based on an arc efficiency of 0.65

Targets	ML algorithms	RMSE	PCC
Linear heat input	Neural network	66.310 J/mm	0.968
	Linear regression	236.675 J/mm	0.7288
	Decision tree	223.163 J/mm	0.7673
	Random forest	175.930 J/mm	0.868
Volumetric energy density	Neural network	4.410 J/mm^3	0.942
	Linear regression	36.191 J/mm^3	0.586
	Decision tree	27.915 J/mm^3	0.689
	Random forest	19.643 J/mm^3	0.795
Deposited layer area	Neural network	1.611 mm^2	0.906
	Linear regression	4.156 mm^2	0.533
	Decision tree	2.812 mm^2	0.814
	Random forest	2.410 mm^2	0.798

Knowledge-based bidirectional thermal variable modelling for directed energy deposition additive manufacturing

Qin, Jian

2024-09-05

Qin J, Taraphdar P, Sun Y, et al., (2024) Knowledge-based bidirectional thermal variable modelling for directed energy deposition additive manufacturing. Virtual and Physical Prototyping, Volume 19, September 2024, Article number e2397008

https://doi.org/10.1080/17452759.2024.2397008